Supporting Information for "Local lydraulic conductivity in heterogeneous porous media"

Quirine Krol [1], Itzhak Fouxon [1,2], Pascal Corso [1], Markus Holzner [1,3,4]

[1]ETH Zurich, Stefano Franscini-Platz 5, 8093 Zurich, Switzerland

[2]Department of Computational Science and Engineering, Yonsei University, Seoul 120-749, South Korea

[3]Swiss Federal Institute for Water Science and Technology EAWAG

[4]Swiss Federal Institute for Forest, Snow and Landscape Research WSL

Contents of this file

1. Direct numerical simulation of Stokes flow in porous media and extraction of pore attributes.

2. Fitting models, results and model performance.

3. Measuring the contribution of the boundary term to Eq.(3).

4. Measuring the Transversal and Longitudinal Energy Dissipation tensor.

5. Histograms of L_{eff} and resistances $\mathcal{R}$.

Introduction

Below we describe the necessary steps and specific settings of the analysis presented in methodology. The fist part consists of the description of the direct numerical simulations performed that are used as a numerical experiment, followed by details of the extraction

of iso pressure surfaces and and their attributes necessary to calculate the pore resistance. The second part gives the details involving models, including a detailed overview of their performance. In the third section we show with an example that Eq.(6) is a reasonable assumption. In the last section we show the distributions of the local resistances and the integrated pore lengths and a very short description of a roadmap describing a possible application of a network model approach.

1. Direct numerical Simulations and extraction of pore attributes

1.1. Geometry of the porous media interface

For all 3 media we have used a levelset of a Gaussian Random Field given by a spectral density as given in (Roberts & Teubner, 1995). Gaussian Random Fields are increasingly used for modeling porous media (Liu et al., 2019). The porous media boundary is given by a level-set and was chosen such that we have porosity values of $0.68, 0.34$ and 0.16, for porous media 1, 2 and 3 respectively. The geometries are represented by 3 stl files that serve as input for the build-in meshing algorithm of Openfoam v. 4.1 Weller, Tabor, Jasak, and Fureby (1998). The bounding box of the porous media (inlet, outlet, upper and lower wall, front and back) are obtained with a BlockMesh. The meshing of the pore space is obtained with SnappyHexMesh with refinement levels 2, for a minimum and 3 for a maximum at the porous media boundary. The number of cells are $35, 31,$ and15 Million respectively.

We inlcuded Table 1.1 that show a few geometrical parameters characterizing the porous media. The averaged pore size is defined by $l_p = 4\phi/s$ with $s = |\Gamma|/V$ the specific surface area given by the ratio of porous media interface total area $|\Gamma|$ and the total volume V. The relative pore size ℓ_p/L, with L the porous media extend. The surface roughness is

defined by the standard deviation of the mean curvature H divided by the average pore size l_p. These measures are introduced to show the wide range of chosen geometries. For example the roughness is smaller for the first porous media compared to the other two. This might indicate that the circularity of the iso-pressure surfaces will be higher, and will have a larger impact on the local hydraulic resistance.

-	porosity	s	l_p/L	$\mathrm{std(H)}^{-1}/\mathrm{l_p}$
PM1	0.68	2.0×10^4	0.17	0.14
PM2	0.34	1.8×10^4	0.08	0.44
PM3	0.17	1.2×10^4	0.06	0.35

1.2. Direct Numerical Simulations

The flow in the three porous medium configurations was simulated using the open-source OpenFOAM software . The three-dimensional meshes consisting in the majority of hexahedral cells were generated from the surface of the porous media represented as a tessellation of triangles. The meshes were obtained using the build-in SnappyHexMesh utility. For the three configurations, the meshes consist of approximately 10 million cells and the non-orthogonality between the faces of each cell is limited to 60and the skewness (as defined within OpenFOAM) of the cells is at most equal to 4 (Moukalled et al., 2016). The steady-state Navier-Stokes equations are resolved using the SIMPLE algorithm for coupling the pressure and momentum equations (Jasak, 1996). Relaxation factors were chosen to be equal to 0.7 for the momentum equation and 0.2 for the pressure equation in order to ensure stability. The choice of the spatial discretization schemes is made such that the simulations are second-order accurate. For the diffusive term, which is dominating for the range of Reynolds numbers considered in these simulations, a limiter for the computation of gradient at the interface between two cells is introduced to take

into account the effect of cell non-orthogonality and skewness and at the same time to keep the solution bounded.

Concerning boundary conditions, the velocity at the pore surface is set to zero. A pressure difference of 1 Pa at the two extremities perpendicular to the stream-wise direction of the box defining the computational domain is imposed. The dimension of the box in this direction is 1 mm. The lateral faces of the computational box are also associated with a zero-velocity condition. The simulations are initialized with PotentialFoam and run with SimpleFoam with standard residual controls of 10^{-6} for both the pressure and velocity fields. The Kinematic viscosity is set to $10^{-6}\mathrm{m}^2\mathrm{s}^{-1}$, which is close to the value for water. The SimpleFoam solver took approximately 20, 8 and 3 hours to obtain the results using 32 cores. A visualization of the results for the three porous media is shown in Fig.2 of the main manuscript.

1.3. Extraction of pores based on iso-pressure surfaces

A chain of VTK-based image analysis techniques Schroeder, Martin, and Lorensen (2006); Hernderson (2007) is employed to extract iso-pressure surfaces. The analysis is scripted with pvpython which comes with the Topology ToolKit (TTK) installation for MACOS High Sierra (python 2.7.15, Paraview 5.4.1, TTK 0.9.3) (Tierny et al., 2018). Specific Paraview/TTK filters are denoted with a capital letter. Values for parameters are given without units, but can be inferred from its definition. Note that the results of the simulation assign p with the kinematic pressure, i.e. in units $\mathrm{m}^2\mathrm{s}^{-2}$, from which the derive the static pressure by multiplication with the fluid density $p_s = p\rho_f$. The results in the paper are in correct units (using Pa for p), but in the following keep p as the kinematic pressure.

Iso-pressure surfaces $\mathcal{S}(p)$ and noise removal

- The iso-pressure surfaces $\mathcal{S}(p)$ are obtained by taking a contour (Contour) filter on pressure value p on the DNS data, see Fig. S1 (left). For porous media 1 and 2 we have chosen k iso-pressure surfaces $p_k = p_0 + k\delta p$ with $\delta p = 5 \times 10^{-6}$. Due to large heterogeneity in the pressure gradient in the third porous media we have chosen to double its resolution to $\delta p = 2.5 \times 10^{-6}$. Due to the noisy edges, as described in the paper, we remove small area patches. This is done by segmenting $\mathcal{S}(p_k)$ with the Connectivity filter in $j \in \{1, M_k\}$ disconnected patches $\mathcal{S}_j(p_k)$ with total area $A_0(p_k)$. Each patch is isolated by a Threshold filter and its surface area $A_j(p_k)$ determined by an IntegrateVariables filter. A maximum value for $A_j(p_k) > A_{\min}$ is used to append (AppendGeometry) to construct $\mathcal{S}(p_k)$ with total area A_{total} consisting of N_k iso-pressure surface patches. The value $A_{\min}$ is determined by a sensitivity study on the total remaining area A_k and the number N_k of remaining patches as a function of $A_{\min}$. The threshold values are $A_{\min} = 3 \times 10^{-11}, 5 \times 10^{-11}$ and 2×10^{-12} for the PM respectively and are determined from Fig. S2 showing A_{total}/A_0 and N/A_0 as a function of $A_{\min}$ for three independent values of p_k. An example of $\mathcal{S}_i$ is shown in Fig. S1 (left). The reduction of the total area has been at most 1.5% for these three test iso-pressure surfaces.

- For $i = 0$ and $i = N$, the iso-pressures surfaces are flat. Since we deem this to be a finite size effect and in this case 'unnatural' we allow the iso-pressure surfaces to develop over the first and last 10 slices, defining p_0.

- To repair some of the irregularities in the surface mesh we employ three more filters: Tetrahydralize, CleantoGrid, and an ExtractSurface.

Segmentation of $\mathcal{S}_i(p_k)$

- To segment $\mathcal{S}_i(p_k)$ into $i \in 1, N_k$ individual pores $\mathcal{S}_i(p_k)$ a connectivity filter is applied (Connectivity, enumeration named 'RegionId'), followed by a ExtractSurface and GenerateSurfaceNormals filter. An example of a segmentation is shown in Fig. S1 (middle).

- To obtain the circularity $\mathcal{C}_i(p_k)$ we take a Contour on numerically zeros velocity $|u| = 10^{-9}$m/s. The obtained contour is subsequently integrated to obtain $\mathcal{L}_i(p_k)$.

By visual inspection of the iso-pressure surfaces (using Paraview software) we see that the circumferences are irregular and will lead to an overestimation of $\mathcal{C}_i(p_k)$. To investigate the dependency of $\mathcal{L}$ on the magnitude $|u|$ we performed a sensitivity study, see Fig.(S2). We found that although the circumferences are visually smoother for higher values of $|u|$ (See third row of Fig S2), fundamental shape features get lost before the smoothing is significant, and can therefore not be used. Choosing $|u| = 10^{-9}$m/s gives us the closest boundary representation of the porous media boundary wall. Choosing $|u| < 10^{-9}$m/s does not lead to higher measured circumferences, this value is therefore numerically zero. Choosing a higher value for the threshold would lead to slightly smoother circumferences (a reduction in $\mathcal{L}$), but with that we also loose qualitative features of the circumferences e.g. a change in topology leads to an increase in the circumferences observed in PM1 and PM2 (See Fig. S2). From this sensitivity study we cannot define a higher value for the threshold that would lead to a better estimate for the circumferences whilst keeping the quality of the shape. Therefore we estimate the error via an alternative method and choose to reduce all the circumferences by this factor.

- **overestimation of $\mathcal{C}_i(p_k)$.** To estimate the order of overestimation regarding $\mathcal{C}_i(p_k)$, we have done a control study by comparing the circumference obtained by thresholding the porous media boundary directly on pressure p_k. This yields a total circumference of

iso-pressure surface $\mathcal{S}(p_k)$. Comparing this to $\sum_i^{N(k)} \mathcal{C}_i(p_k)$, with $N(k)$ the total number of iso-pressure pathces of iso-pressure surface $\mathcal{S}(p_k)$, gives us an averaged overestimation of $\mathcal{C}_i(p_k)$ by a factor $\epsilon = 1.15 \pm .01, 1.11 \pm .01$, and $1.08 \pm .04$, for the three porous media respectively. This estimate is based on 40 iso-pressure surfaces taken from each porous media.

- For each $\mathcal{S}_i(p_k)$ we integrate (IntegrateVariables) the surface to extract the averaged position $\mathrm{X}_i(p_k)$, total flux $Q_i(p_k) = \int_{\mathcal{S}_i(p_k)} \mathbf{u} \cdot \mathbf{n}\, da$, and total area $A_{i,j} = \int_{\mathcal{S}_i(p_k)} da$ and circularity $\mathcal{C}_i(p_k) = \mathcal{L}_i^2(p_k)/(4\pi A_i(p_k))$.

Local inheritance $\mathcal{S}_i(p)$

Goal: For each $\mathcal{S}_i(p_k)$ finding its closest neighbor $\mathcal{S}_j(p_k + \delta p)$.

-]This neighboring iso-pressure patch (building up a pore) is found by calculating the distance function $f_d(\mathbf{x}, \mathcal{S})$, between point $\mathbf{x} \in \mathcal{S}_i(p_k)$ and all iso-pressure patches $\mathcal{S}_l(p_k + dp)$. This distance function is calculated by the vtkDistancePolyDataFilter, a programmable vtk filter, and is defined by

$$f_d\left(\mathbf{x}, \mathcal{S}\right) = \min\{\|\mathbf{x} - \mathbf{y}\|\} | \mathbf{y} \in \mathcal{S}. \tag{1}$$

for each i, l we define the averaged distance matrix by using the IntegrateVariables filter

$$d_{i,l}(p_k) = \frac{1}{A_i(p_k)} \int_{\mathcal{S}_i(p_k)} f_d(\mathbf{x}_i, \mathcal{S}_l(p_k + \delta p))\, dS_i. \tag{2}$$

The closest neighbor $\mathcal{S}_j(p_k+\delta p)$ is found by the minimum value of $d_{i,j}(p_k) = \min\{\mathrm{d_{i,l}(p_k)}\}$. The closest neighbor is assigned by the identification number of the nearest neighbor $n_i(p_k) = j$

- Subsequently we compute the change in surface area $dA_i(p_k) = A_i(p_k) - A_j(p_k + \delta p)$, the averaged location of the neighboring pore $\mathbf{X}_i^n(p_k) = \mathbf{X}_j(p_k + \delta p)$ and the distances

between the two averaged coordinates $dX_i(p_k) = |\mathbf{X}_i(p_k) - \mathbf{X}_j(p_k + \delta p)|$. Last but not least we assign $dx_i(p_k) = d_{i,j}(p_k)$, which is used as dx in the Eq. (10) and (12).

- Now each patch $\mathcal{S}_i(p_k)$ has intrinsic attributes enlisted: $i, n_i, \mathbf{X}_i$, Q_i, A_i, $\mathcal{C}_i$. Additionally it has attributes that depend on its nearest neighbor n_i, $\mathbf{X}_i^n$, dA_i, dx_i and dX_i. For all these attributes p_k is implied. The intrinsic attributes of the nearest neighbor are added to the attributes of $\mathcal{S}_i(p_k)$ for convenience.

- It is important to notice the difference between dx_i and dX_i. The former is the averaged distance between two iso-pressure surface patches and therefore assigned to dx wich stems from $dV = Adx$. The latter is the distance between the two averaged positions of the iso-pressure patches.

- Gathered all necessary pore attributes, we can use a least-squared fit of Eq.(9) to obtain α_i and Eq.(15) to obtain α and β.

Defining pores by integration of local inheritance of $\mathcal{S}_i(p)$

• For the first iso-pressure patches $S_i(p_0)$ we initiate a pore identification number $P_i(p_k) = i$.

• For each pore i we integrate to the nearest neighbor j by assigning the same pore number to $\mathcal{S}_{n_i}(p_0 + \delta p) : P_{n_i}(p_0 + \delta p) = i$. This forward integration takes place only when five quality factors are fulfilled,

• $Q_1 = (|dX_i - dX_{n_i}|)/dX_i < q_1$: Ensuring that there is no abrupt change in consecutive averaged distances.

• $Q_2 = |dA_i|/A_i < q_2$: Ensuring no abrupt changes in the surface area of consecutive area patches.

• $Q_3 = (|Q_{0,j} - Q_{1,nn_{i,j}}|)/Q_{1,nn_{i,j}} < q_3$: Ensuring that the flux is 'nearly' conserved.

• $Q_4 = dX_i < q_4$: Ensuring that pores split if they are too far apart.

• $Q_5 = A_i > q_5$: Removing 'small' area patches. The values are found by trial and error to decrease the number of pores but still capturing the merging and splitting of pores. For each quality factor we have 3 values tailored to each porous media 1,2 and 3 independently. For $q_1 = [1.6, .4, .4]$, $q_2 = [.5, .5, 1]$, $q_3 = [.2, .2, 1]$, $q_4 = [10^{-5}, 10^{-5}, 9 \times 10^{-5}]$ and $q_5 = [1 \times 10^{-10}, 1 \times 10^{-10}, 5 \times 10^{-11}]$ These requirement seem quite loose, but have proven to be quite effective, see Fig. S1 (Right).

• The assignment of pore numbers can continue iteratively until all patches have a pore identification number $P_i(p_k)$.

- For all P_i we can calculate Eq.(12) and Eq.(15).

2. Fitting models, Results and Performance

2.1. Fitting models

In the paper we have fitted four models f_i

$$\frac{dp}{dx} = \frac{Q}{A^2} f_i \tag{3}$$

for all consecutive pore patches that comply with the the quality factors Q_i, not to be mistaken with averaged flux. Since the data is spread over multiple orders of magnitude, we obtained a least squared fit by taking the logarithm on either side of the equation

$$\log\left[\frac{dp}{dx}\right] = \log\left[\frac{Q}{A^2} f_i\right] \tag{4}$$

The 4 functions that have been fitted are given by

$$f_{\mathrm{HP}} = \quad 1$$

$$f_1 = \quad \alpha_0 + \alpha_1 \mathcal{C} + \alpha_2 \frac{1}{A} \left|\frac{dA}{dx}\right|^2$$

$$f_2 = \beta_0 + \beta_1 \mathcal{C}$$

$$f_3 = 1 - \alpha \left[1 - (\mathcal{C}/\epsilon)^{\beta}\right].$$

$$f_4 = \gamma_0 + \gamma_1 (\mathcal{C}/\epsilon) + \gamma_1 (\mathcal{C}/\epsilon)^2 .$$

For f_3 and f_4 we have used an overall correction factor for $\mathcal{C}$ specific to each porous media as reported in the paper. We have included one additional condition that $dp/dx > 0.8\frac{Q}{A^2}$, to ensure that unphysical measurements of the pressure gradient. This can be caused by wrongly matched patches. This led to a reduction in evaluated surface areas of 0.4%, 0.3% and 2.6% for the porous media respectively. In addition singular patches that have not been matches are contributing to respectively $18\%, 26\%$ and 1.7% of the evaluated surface areas.

2.2. Results 1

Summary of fitting parameters and error measures for porous media 1

model	parameters	relative contributions	R^2
f_{HP}	-	$[100\%]$	0.91
f_1	$\alpha_0 = 0.48, \alpha_1 = 0.90, \alpha_2 = -6.3 \times 10^{-7}$	$[23\%, 77\%, < .1\%]$	0.98
f_2	$\beta_0 = 0.48, \beta_1 = 0.90$	$[23\%, 77\%]$	0.97
f_3	$\alpha = 0.45, \beta = 1.09$	-	0.97
f_4	$\gamma_0 = 0.53, \gamma_1 = 1.18, \gamma_2 = 9.5 \times 10^{-3}$	$[25\%, 73\%, 1\%]$	0.98

Summary of fitting parameters and error measures for porous media 2

model	parameters	relative contributions	R^2
f_{HP}	-	$[100\%]$	0.97
f_1	$\alpha_0 = 0.52, \alpha_1 = 0.87, \alpha_2 = 1.1 \times 10^{-6}$	$[31\%, 69\%, < .1\%]$	0.99
f_2	$\beta_0 = 0.52, \beta_1 = 0.87$	$[31\%, 69\%]$	0.99
f_3	$\alpha = 0.58, \beta = 1.05$	-	0.98
f_4	$\gamma_0 = 0.71, \gamma_1 = 0.65, \gamma_2 = 0.06$	$[42\%, 51\%, 8\%]$	0.99

Summary of fitting parameters and error measures for porous media 3

model	parameters	relative contributions	R^2
f_{HP}	-	$[100\%]$	0.94
f_1	$\alpha_0 = 0.26, \alpha_1 = 1.07, \alpha_2 = 6.3 \times 10^{-5}$	$[18\%, 82\%, < .1\%]$	0.97
f_2	$\beta_0 = 0.26, \beta_1 = 1.07$	$[18\%, 82\%]$	0.97
f_3	$\alpha = 0.34, \beta = 1.08$	-	0.97
f_4	$\gamma_0 = 2.1, \gamma_1 = -2.1, \gamma_2 = 1.4$	$[148\%, -136\%, 88\%]$	0.96

2.3. Results 2

The model performance have been expressed in the Pearson correlation coefficient R^2 of the measured $\mathcal{R}_{\mathrm{meas}} = \Delta p/Q$ and the modeled,

$$\mathcal{R}_{\mathrm{m}}(f_i) = \int_0^{L_{\mathrm{eff}}} \frac{1}{A^2} f_i(\mathcal{C})\, dx, \tag{5}$$

and the HP model

$$\mathcal{R}_{\mathrm{HP}} = \int_0^{L_{\mathrm{eff}}} \frac{1}{A^2}\, dx. \tag{6}$$

Since the errors between $\mathcal{R}_{\mathrm{meas}}$ and $\mathcal{R}_{\mathrm{HP}}$ shows a high degree of heteroscedasticy (Wilcox, 2009), the Pearson correlation function is not adequate to compare these models, therefore we also computed the root-mean-square-relative error (RMSRE). To investigate the potential improvement on preferential channels (those with low resistances or high fluxes), we weighted the RMSRE with the total flux Q through the pore, $\mathrm{RMSRE_Q}$. The results are shown in the following tables for the three porous media respectively.

Summary model hydraulic resistance performance for porous media 1:

model	R^2	RMSRE	$\mathrm{RMSRE_Q}$
$\mathcal{R}_{\mathrm{HP}}$	0.91	0.59	0.86
$\mathcal{R}_{\mathrm{m}}(f_2)$	0.97	0.12	0.10
$\mathcal{R}_{\mathrm{m}}(f_3)$	0.97	0.32	0.27

Summary model hydraulic resistance performance for porous media 2:

model	R^2	RMSRE	RMSRE_Q
$\mathcal{R}_\text{HP}$	0.88	0.48	0.61
$\mathcal{R}_\text{m}(f_2)$	0.95	0.14	0.13
$\mathcal{R}_\text{m}(f_3)$	0.95	0.28	0.29

Summary model hydraulic resistance performance for porous media 3:

model	R^2	RMSRE	RMSRE_Q
$\mathcal{R}_\text{HP}$	0.99	0.32	0.32
$\mathcal{R}_\text{m}(f_2)$	0.99	0.17	0.15
$\mathcal{R}_\text{m}(f_3)$	0.99	0.28	0.20

3. Measuring the relative contribution of the boundary term to Eq.(3)

In this section we estimate the relative contribution of the first term of the right-hand side of Eq.(3) of the manuscript, given by

$$Q\Delta p = -\mu \int_{S_{p_1}+S_{p_2}} \mathbf{u}\cdot(\nabla\otimes\mathbf{u})\mathbf{n}\, dS + \mu\int_{\mathcal{V}}(\nabla\otimes\mathbf{u})^2 dV. \tag{7}$$

We manually selected 10 pores (5 for porous media 1, 4 for porous media 2 and one for porous media number 3), and measured the ratio of the absolute value of the first term of the right-hand side and the left-hand side of the equation.

$$\text{ratio} = \frac{\left|-\mu \int_{\text{S}_{\text{p}_1}+\text{S}_{\text{p}_2}} \mathbf{u}\cdot(\nabla\otimes\mathbf{u})\mathbf{n}\,\text{dS}\right|}{\text{Q}\Delta\text{p}} \tag{8}$$

for varying lengths of the pore. Using a gradient filter, GradientOfUnstructuredDataSet, to extract the dissipation tensor $\partial_i u_j$. Note that gradients aren't used throughout the methods in this paper because they are less reliable since the the gradients increase the noise compared to the noise of the velocity data (see next section). Since the noise on the gradients lead to an overestimation of the ratio. This is not problematic for this purpose since we search for an upper value for its contribution. We have plotted all possible

lengths that fit within one pore e.g. if a pore comprises 20 pores, we can measure 5 pores of length 15, by moving the window. In Fig. S3 we have plotted the ratio of the first term for all possible pores (left) with varying pore size for 10 available pores with respect to the left-hand side of the equation $Q\Delta p$. In Fig.3 (right) we have plotted the averaged ratios. We find that almost all ratios are well below 10% and that on average the ratio is below 5%. Almost all pores show that this ratio decreases roughly exponentially, reducing by half after a pore length of 7-10 units. Pore lengths are here expressed in Δp.

4. Measuring the relative Longitudinal and Transversal energy dissipation on an iso-pressure surface

In the theoretical section of the paper we have derived expressions for the longitudinal and transversal energy dissipation tensors, by

$$|\nabla_i u_j|^2 \approx |\nabla_s u_p|^2 + |\nabla_n u_p|^2 . \tag{9}$$

where we have assumed that the terms $|\nabla_n u_n|^2$ and $|\nabla_s u_n|^2$ are negligible. We will show two examples where we have calculated the individual terms of the total viscous dissipation. Because the highest dissipation is expected to be located near the porous media interface and the discretization also refined at the interface the numerical noise is also expected to be higher, see Fig S4. All 3 porous media contain some points in the mesh where the VTK gradient filter can't factorize the linear system which leads to very high values of the respected fields, See fig S4. The origin lies likely in the mesh quality generated by the snappyHexMesh generator contained in the openFoam simulation. Since the simulations have all converged we do not question the original simulation results but we do note that post-processing of these meshes can be difficult especially if gradients have to be calculated. Nevertheless we have tried to quantify the relevance of the transversal

and longitudinal terms of the viscous dissipation tensor. We have chosen to threshold the unreasonable high gradient terms based on outliers in the histograms of the gradients. For the first porous media the porous media the refinement was chosen a degree higher than the others, and led to 'nan' results of the integrated relative contributions. For the two other porous media we have found reasonable results given in Table S3. Since we have to filter out quit some data that exhibits unreasonable high values the percentages are not adding up to 100%. By visual inspection we can examine the term $|\nabla_i u_j|^2$ in all porous media and we see that the total dissipation correlates with gradients in the transverse direction. Also in this data we can see that for Porous Media 3 the relative contribution of the longitudinal term $|\nabla_n u_p|^2$, 24% is in the same order as the transversal term $|\nabla_s u_p|^2$ which amounts to 32%. This observation is in agreement with the fitting of the two contributions in the paper, See Table S1.

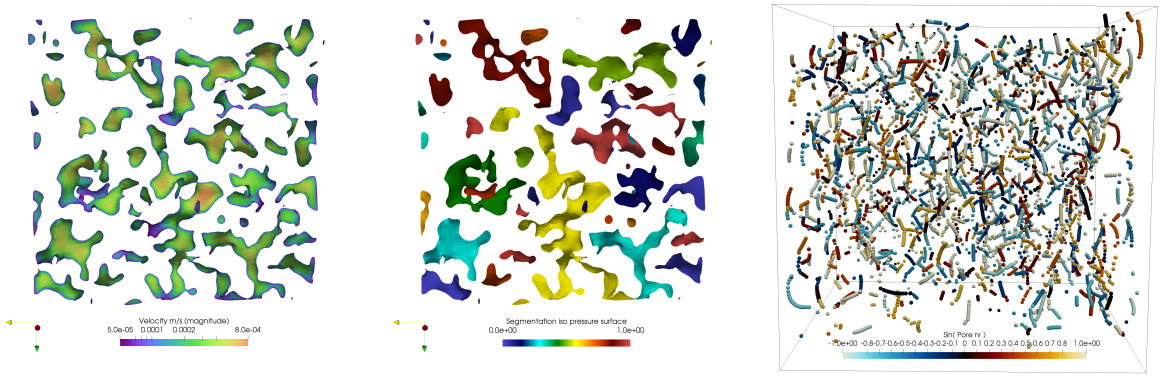

Figure S1. Visualization of left: velocity field $|\mathbf{u}|$of an iso-pressure surface $\mathcal{S}(p)$ at pressure value p, middle: segmentation into iso-pressure patches $\mathcal{S}_i(p)$, right: Pore identification throughout the porous medium.

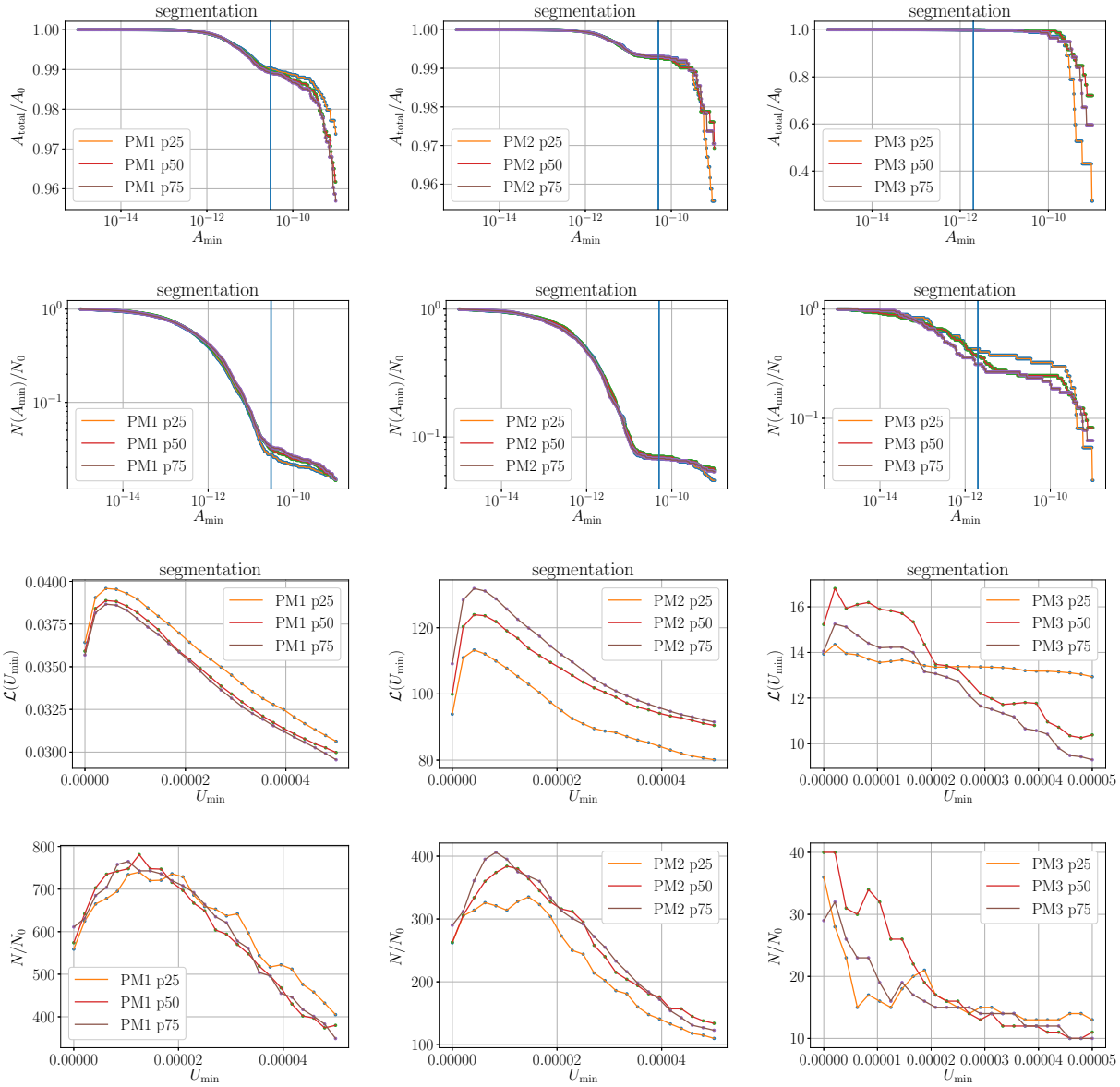

Figure S2. First row: Sensitivity study of total area A as a function of A_{min}. Second row: Sensitivity study of the number of patches N as a function of A_{min}. Third row: Sensitivity study of the total length of the circumference of three the iso-pressure surfaces $\mathcal{S}(p)$, $\mathcal{L}$ as a function of U_{min}. Fourth row: Sensitivity study of the total number of iso-pressure 'patches' $\mathcal{S}_i(p)$, N as a function of U_{min}.

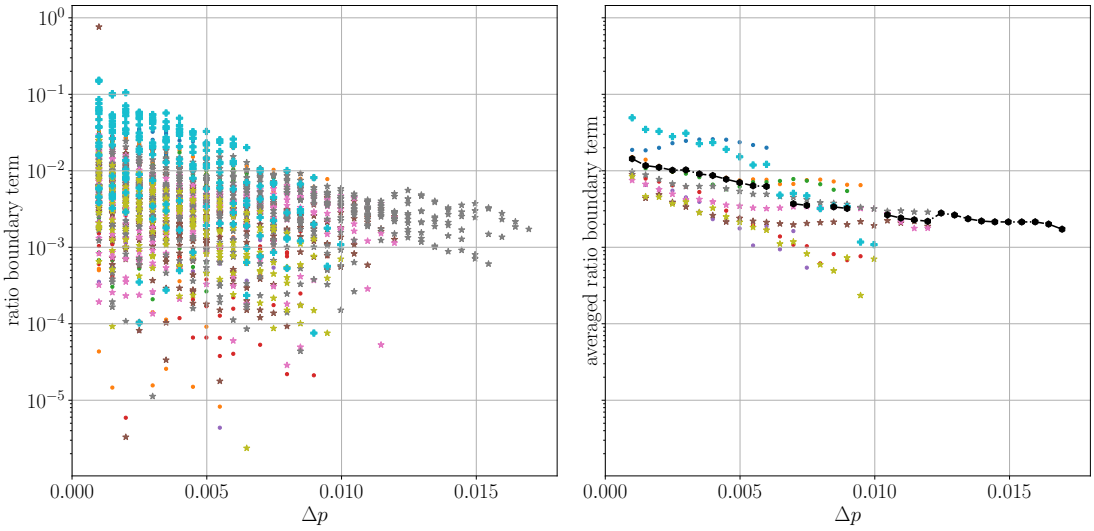

Figure S3. Left: Ratio of the boundary term to $Q\Delta p$ (first term of the right-hand side of Eq.(3) of the manuscript) as a function of the pore length (expressed in Δp) for 10 pores (bullets for pores from PM1, stars for pores from PM2, and squares for the pore of PM2). Right: The averaged ratio (averaged over all pore lengths within one pore (term 2 of the right-hand-side) as a function of pore length. In black the averaged value over all pores.

PM	$\lvert\nabla_s u_p\rvert^2$	$\lvert\nabla_n u_p\rvert^2$	$\lvert\nabla_n u_n\rvert^2$	$\lvert\nabla_n u_n\rvert^2$
PM2	71%	17%	12%	12%
PM3	32%	24%	10%	5%

Table S1. Estimated relative contributions to the total viscous dissipation on an iso-pressure surface.

5. Histograms of $\mathcal{R}$ and L_{eff}

In Fig. S5 we plotted the histograms of measured hydraulic resistances $\mathcal{R}_{\text{meas}}$, HP model $\mathcal{R}_{\text{HP}}$, and our model $\mathcal{R}_{\text{m}}(f_2)$. In Fig. S6 we have shown the histograms of L_{eff}. The plots include a Kernal Density Estimate (KDE) of the distributions. These distributions could potentially be

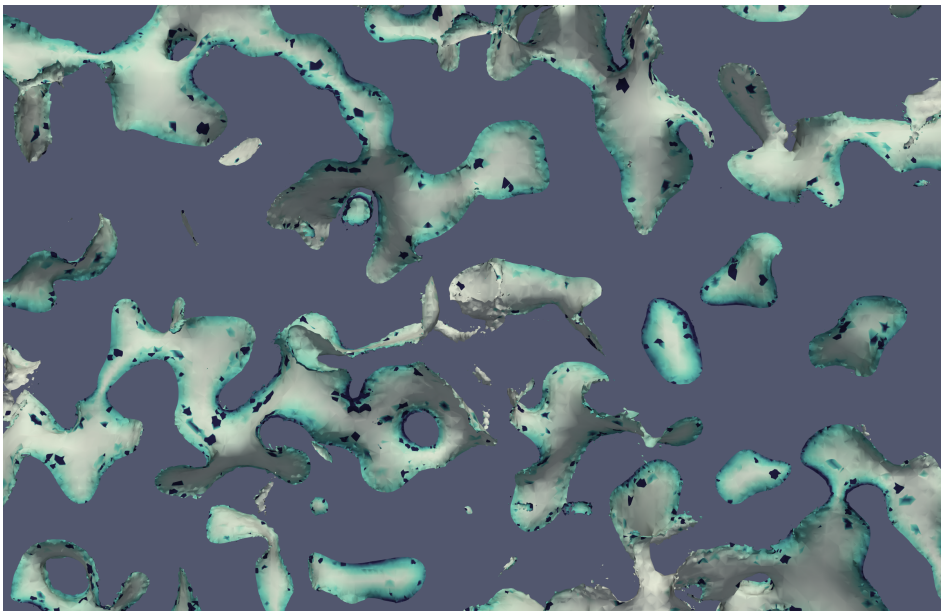

Figure S4. A visualization of the energy dissipation tensor $|\nabla \otimes \mathbf{u}|$ on a iso-pressure surface of PM1, indicating the numerical issues that are accompanied by gradients of the velocity vector.

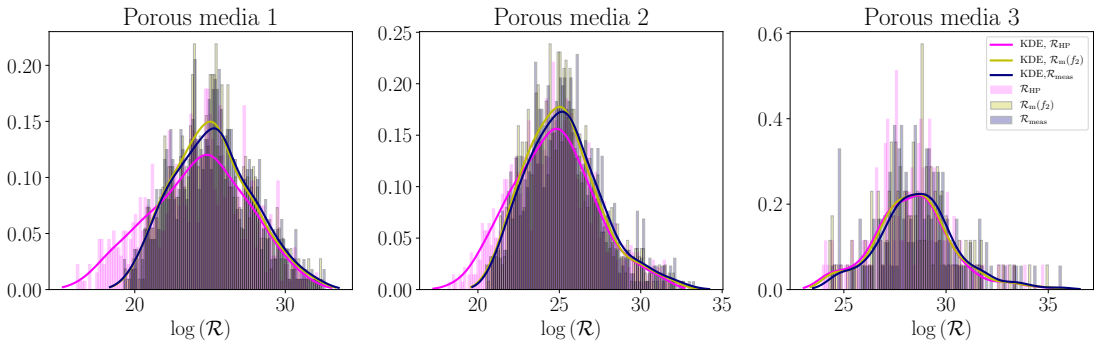

Figure S5. Histograms of the measured $\mathcal{R}_{\text{meas}}$, $\mathcal{R}_{\text{HP}}$ and $\mathcal{R}_{\text{m}}(f_2)$.

used to build a statistical network with equivalent network topology, with each bond representing a pore with a stochastic resistance drawn from these distributions.

References

Hernderson, A. (2007). *ParaView Guide, A Parallel Visualization Application.*

Jasak, H. (1996, January). Error analysis and estimation for the finite volume method with

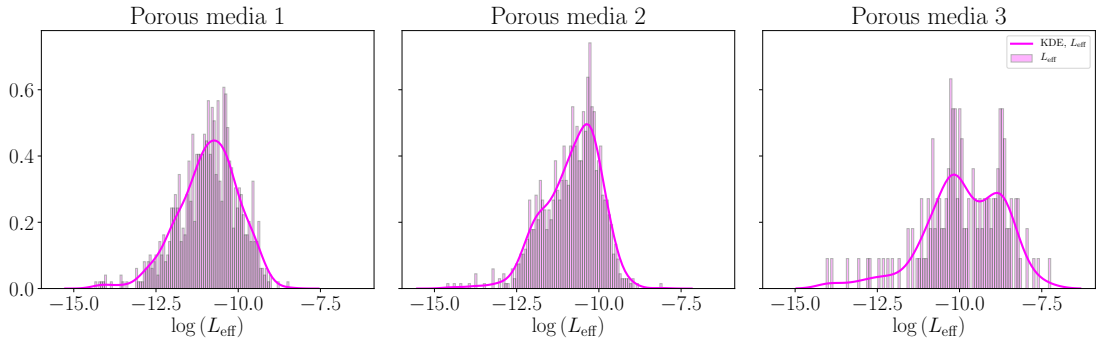

Figure S6. Histograms of the measured pore sizes L_{eff} and the KDE estimate.

applications to fluid flows.

Liu, Y., Li, J., Sun, S., & Yu, B. (2019, October). Advances in Gaussian random field generation: A review. *Comput Geosci*, *23*(5), 1011–1047. doi: 10.1007/s10596-019-09867-y

Moukalled, F., Mangani, L., & Darwish, M. (2016). *The Finite Volume Method in Computational Fluid Dynamics: An Advanced Introduction with OpenFOAM® and Matlab*. Springer International Publishing. doi: 10.1007/978-3-319-16874-6

Roberts, A., & Teubner, M. (1995, May). Transport properties of heterogeneous materials derived from Gaussian random fields: Bounds and Simulation. *Physical Review E*, *51*(5), 4141–4154. doi: 10.1103/PhysRevE.51.4141

Schroeder, W., Martin, K., & Lorensen, B. (2006). *The visualization toolkit: An object-oriented approach to 3D graphics* (4. ed ed.). Clifton Park, NY: Kitware, Inc.

Tierny, J., Favelier, G., Levine, J. A., Gueunet, C., & Michaux, M. (2018, January). The Topology ToolKit. *IEEE Transactions on Visualization and Computer Graphics*, *24*(1), 832–842. doi: 10.1109/TVCG.2017.2743938

Weller, H. G., Tabor, G., Jasak, H., & Fureby, C. (1998, December). A tensorial approach to computational continuum mechanics using object-oriented techniques. *Computers in*

Physics, *12*(6), 620. doi: 10.1063/1.168744

Wilcox, R. R. (2009, November). Comparing Pearson Correlations: Dealing with Heteroscedasticity and Nonnormality. *Communications in Statistics - Simulation and Computation*, *38*(10), 2220–2234. doi: 10.1080/03610910903289151